Conductivity and hydration trends in disordered fluorite and pyrochlore oxides: A study on lanthanum cerate-zirconate based compounds

Vasileios Besikiotis[1], Sandrine Ricote[2], Molly Hjorth Jensen[2], Truls Norby[1], Reidar Haugsrud[1]

[1] Department of Chemistry, University of Oslo, FERMiO, Gaustadallèen 21, NO-0349 Oslo, Norway

[2] Department of Energy Conversion and Storage, Technical University of Denmark, Frederiksborgvej 399, DK-4000 Roskilde, Denmark

Abstract

In the present contribution we discuss the influence of order/disorder on the concentration and mobility of ionic charge carriers in undoped and acceptor (calcium) doped fluorite and pyrochlore structured lanthanum cerate-zirconate solid solutions: $(La_{1-y}Ca_y)_2(Ce_{1-x}Zr_x)_2O_{7-\delta}$ (y=0, 0.02, 0.10; x=0, 0.50, 0.75). Characterization of the electrical conductivity as a function of temperature and oxygen partial pressure revealed contribution from electronic carriers in reducing atmosphere, but otherwise these materials are ionic conductors. Oxide ion conductivity dominates at high temperatures while protons become more dominating as charge carrier at temperatures below typically 500 °C under wet conditions. The hydration enthalpies were determined by simultaneous thermogravimetry and differential scanning calorimetry (TG-DSC). The contribution from ionic conductivity increases and the hydration enthalpy becomes more exothermic with higher cerium content, i.e. with more disordered materials. The proton conductivity decreases upon acceptor substitution of La^{3+} with Ca^{2+} which is attributed to trapping of the charge carriers by the effectively negative acceptor.

Key words*: proton conductivity, disorder, pyrochlores, fluorites, isotope effect, TG-DSC*

Introduction

Solid Oxide Fuel Cells (SOFCs) can be divided into the "classical" SOFCs where the charge carriers are oxide ions and the proton conducting SOFCs (PC-SOFCs or PCFCs) where protons are the charge carriers. Despite the relatively mature state of SOFC technology, PCFCs exhibit potential advantages encouraging their development. One of the most important is that water forms on the cathode side rather than on the anode side during operation, which reduces fuel dilution and increases fuel utilization.

State-of-the-art high temperature proton conductors comprise alkaline earth perovskites such as acceptor-doped $BaCeO_3$, $SrCeO_3$ [1, 2], $BaZrO_3$ [3, 4], and $BaCeO_3$-$BaZrO_3$ solid solution [5]. However, the applicability of these is hampered by complex fabrication, high grain boundary resistance and reactivity towards CO_2 and H_2O. Lanthanide based systems are expected to show better chemical stability [6-11], where the family of lanthanide based pyrochlore/fluorite structured proton conductors, Ca^{2+}-doped $La_2Zr_2O_7$ has been reported to have high proton transport numbers in the temperature range 200-600 °C [12]. Still the proton conductivity is close to two orders of magnitude lower than in the state-of-the-art perovskites. Tao *et al.* [13] used acceptor-doped $La_2Ce_2O_7$ as an electrolyte showing stability under CO_2. Lin *et al*. [14] tested $La_2Ce_2O_7$ as an electrode component for a Ca^{2+}-doped $LaNbO_4$ based PCFC revealing good catalytic activity towards oxygen splitting.

Generally the degree of cation order/disorder is essential to the functional properties of materials in the pyrochlore/fluorite system. For disordered fluorites (Fig. 1a) the arrangement of the A and B site cations is random whereas the cations are ordered for the pyrochlores (Fig. 1b). In the case of the pyrochlores, the 8*a* Wyckoff position is unoccupied, whereas for the disordered fluorites, 7 oxygen anions are distributed over 8 equivalent sites leaving one vacant site. The ratio of the ionic radius of the 8-coordinated A-site cation ($r_{A^{3+}}$) to that of the 6-coordinated B-site cation ($r_{B^{4+}}$) governs the extent of cation disorder in pyrochlores. The stability field of the structure for zirconates and titanates has been established in the range $1.46 \le r_{A^{3+}}/r_{B^{4+}} \le 1.80$ [15, 16]. As the ratio

$r_{A^{3+}}/r_{B^{4+}}$ decreases, cation disorder increases and transition to the fluorite eventually occurs. In order to qualitatively express the degree of the cation order in the studied series of materials herein, we define an empirical cation order factor φ based on the ratio of the radii of the A and B cations,

$$\varphi = \left(\frac{r_{A^{3+}}}{r_{B^{4+}}} - 1.33 \right) \cdot 3.57 \qquad (1)$$

where $r_{A^{3+}}$ and $r_{B^{4+}}$ are the Shannon radii of A and B cations in $A_2B_2O_7$. When φ is 0 the system is fully disordered and when φ is 1 it is fully ordered.

In this contribution we attempt to rationalize the effects of order/disorder and acceptor doping on the hydration thermodynamics and ionic conductivity in the $(La_{1-y}Ca_y)_2(Ce_{1-x}Zr_x)_2O_{7-\delta}$ (y=0, 0.02, 0.10 and x=0, 0.50, 0.75) series. $La_2Ce_2O_7$ crystallizes as a disordered fluorite [17] with $r_{A^{3+}}/r_{B^{4+}}$ = 1.33, and when substituting part of the Ce^{4+} with Zr^{4+}, the ratio $r_{A^{3+}}/r_{B^{4+}}$ increases, leading to a more ordered system where the pyrochlore structure is adopted. Table 1 summarizes the φ values of each studied system, as well as for $La_2Zr_2O_7$ and, moreover, the corresponding abbreviation for the different compositions. The hydration thermodynamics were derived using simultaneous thermogravimetry and differential scanning calorimetry (TG-DSC) as described in [18], and the electrical characterization was performed by means of electrochemical impedance spectroscopy (EIS).

2. Experimental

Two different routes were followed during synthesis of the materials: a citric acid route and the ceramic method. LC was synthesized by dissolving La and Ce nitrates in distilled water and stabilizing the cations in solution by addition of citric acid (metal nitrate: citric acid molar ratio 1:1). The solution was then heated for 5 h at 225 °C. The obtained Xerox gel was ground in a mortar and calcined for 6 h at 900 °C. The resulting powder was milled in an agate planetary mill for 20 min, pressed into pellets with a 20 mm die at 150 MPa, and finally sintered at 1500 °C for 6 h yielding pellets with a relative density of ~95 % as estimated from the volume and mass of the specimen. (La_{1-}

$_yCa_y)_2(Ce_{1-x}Zr_x)_2O_{7-\delta}$ (y=0, 0.02, 0.10 and x=0, 0.50, 0.75) were prepared by solid state reaction, mixing by ball milling in ethanol for 20 h stoichiometric quantities of dried oxide precursors: La_2O_3 (Sigma Aldrich, 99.9 % trace metals basis), CeO_2 (Aldrich, 99 %, trace of metal basis, <5 μm), ZrO_2 (Tosoh TZ-0) and $CaCO_3$ (Fluka, purity>99 %). The dried mixtures were pelletized and heated in air at 1100 °C for 6 h. This step was repeated twice with intermediate crushing in a mortar. After the third calcination, the powders were ball milled in ethanol for 20 h, dried, and pellets were made by uniaxial pressing at 55 MPa and cold isostatic pressing 300 MPa. Finally the green pellets were sintered in air at 1600 °C for 12 h. The relative density estimated from the volume and mass of the sintered body was ~94 %.

Structural characterization of the pellets was done by X-ray diffraction (XRD), with a STOE 2θ or a Siemens D5000 using $CuK_{\alpha 1}$ radiation. The diffractograms were refined using the Le Bail method [19] implemented in the *FullProf Suite* [20] or with the cell refinement option of the *WinXPOW* software [21].

Prior to the conductivity measurements, circular Pt electrodes were painted onto both faces of the specimen (Metalor Technologies SA) and fired at 1100 °C for 1 h. Electrochemical impedance spectroscopy (EIS) was performed in the temperature range 250-1000 °C using Novocontrol alpha A or Solartron 1260 frequency response analyzers, in the frequency range 1 Hz to 1 MHz and with an oscillation of 0.2 V rms. The total conductivity was measured at constant frequency (10 kHz) during temperature ramps between 800 and 300 °C in dry (30 ppm H_2O) and moisturized (0.025 atm H_2O or 0.022 atm D_2O) oxygen containing atmospheres. It was confirmed that the total conductivity measured during these temperature ramps represents bulk properties of the materials by comparing it to bulk values from deconvoluted impedance spectra taken every 50 °C between 800 and 300 °C. Additionally, conductivity isotherms were measured versus oxygen partial pressure in wet atmosphere (0.025 atm H_2O), using mixtures of O_2 or air and N_2 for oxidizing atmospheres and mixtures of H_2 and N_2 for reducing atmospheres. Impedance spectra were fitted to a series of (*RQ*) circuits, using the *Equivalent circuit for Windows* software [22], where (*RQ*) denotes a resistor and a constant phase element (CPE) in parallel. Prior to fitting, 5 pF representing approximately the parasitic capacitance

of the measurement setup was subtracted from the raw data. In order to relate the different contributions of the impedance spectra to physical processes, the pseudo-capacitances, C_i, of the sub-circuits were calculated using:

$$C_i = Y_i^{\frac{1}{n_i}} \cdot R_i^{\frac{1}{n_i}-1} \quad (2)$$

Y_i and n_i define the admittance of the CPE given by $Y_Q = Y_i \cdot (\mathrm{j}\omega)^{n_i}$, where ω is the angular frequency and $\mathrm{j} = \sqrt{-1}$ [23]. Before fitting the recorded spectra, the obtained data were validated by means of Kramers-Kronig (KK) transformation tests as included in the software [24]. The χ^2 values of the K-K transformation, as well as for the fitting of the model equivalent circuits to the spectra, were in the order of 10^{-6}-10^{-7}.

Standard molar hydration enthalpies were determined isothermally as a function of the water vapor pressure on powder from crushed pellets with a TG-DSC (Netzsch Simultaneous Thermal Analyzer 449C Jupiter) at 600 °C. For more details on the TG-DSC methodology the reader is referred to refs. [18, 25]. TG-DSC was carried out at both 600 and 400 °C to minimize any uncertainties on the obtained hydration enthalpies and water uptake.

3. Results

3.1. Structural and compositional characterization

Fig. 2a presents the XRD patterns of the as prepared materials. The XRD patterns and the Le Bail fit showed that the as prepared systems adopt the pyrochlore (space group $Fd\bar{3}m$) or the disordered fluorite structure (space group $Fm\bar{3}m$). As demonstrated in [17], LC crystallizes in the disordered fluorite structure with $r_{A^{3+}}/r_{B^{4+}}$ = 1.33. Ca02LCZ50 and LCZ50 ($r_{A^{3+}}/r_{B^{4+}}$ =1.46), and

Ca10LCZ50 ($r_{A^{3+}}/r_{B^{4+}}$=1.45), on the other hand, lie at the border between disordered fluorite and pyrochlore. Compounds with higher levels of zirconium, Ca02LCZ75 and Ca10LCZ75 ($r_{A^{3+}}/r_{B^{4+}}$ =1.53), crystallize in the pyrochlore structure. In both the latter nominal compositions a secondary phase was present, marked with an asterisk in Fig. 2. In the ICDD data base, this secondary phase was identified and denoted as a $La_{1-x}Zr_xO_{2-\delta}$ fluorite, whose 'x' value was estimated by us to be 0.45 from the Vegard's law.

Fig. 2b depicts the XRD patterns of Ca02LCZ50 and Ca02LCZ75 in the 2θ° range of 54.5-59.0°. The (622) and (444) peaks are shifted towards higher angles with increasing zirconium content, reflecting the change in average ionic radius of the B site. Indeed, zirconium cations are smaller than cerium cations, so the increase in the zirconium content leads to smaller lattice parameters and a higher $r_{A^{3+}}/r_{B^{4+}}$ ratio which, according to eq. 1, will increase the order of the system.

3.2 Electrical measurements

Fig. 3. displays the impedance spectra of Ca02LCZ50 and Ca10LCZ50 recorded at 400 °C under wet O_2. The spectra were fitted using an $(R_1Q_1)(R_2Q_2)$ circuit. The capacitance of the sample was measured at room temperature in a cell free of stray capacitance and was found to be $5\cdot10^{-12}$ F; this corresponds to a relative dielectric constant of circa 22. On this basis, the first element (R_1Q_1), having a pseudo capacitance equivalent of $3\text{-}4\cdot10^{-11}$ F·cm^{-1} is ascribed to the bulk. The pseudo capacitances of the other semi-circle, C_2, were in the order of $3\cdot10^{-5}$ F·cm^{-1} and were assigned to processes at the electrodes. Notably, the grain boundary contribution to the impedance is here negligible - similar as for all the studied systems.

Fig. 4 shows the dependence on the total conductivity of the oxygen partial pressure at 800 °C, pH$_2$O = 0.025 atm. The total conductivity is dependent of the oxygen partial pressure under reducing conditions and is increasing with decreasing oxygen partial pressure. Under sufficiently oxidizing conditions there is also a slight increase in the conductivity values upon increasing pO$_2$, but

insignificant compared to the effect in reducing atmospheres. These two regimes indicate that the conductivity is dominated by electrons under reducing conditions and by ions otherwise. As a result, the total conductivity measured under oxidizing conditions is assumed to reflect predominantly ionic conductivity in what follows.

Based on the difference in mass of the hydrogen isotopes, effects of H-D isotope exchange on the total conductivity were used to discriminate between conditions where protons and oxide ions are the major charge carriers [26, 27]. In Fig. 5 (left axes) we compare the temperature dependence of the ionic conductivity for LCZ50 in O_2 either with 0.025 atm H_2O or 0.022 atm D_2O. The isotope effect increases gradually below 650 °C, as emphasized by the increase of $\sigma_{H_2O} / \sigma_{D_2O}$ (right axes Fig. 5) and the increase in the activation energy by 0.079 eV from H_2O to D_2O in the temperature range 500-300 °C, revealing the protonic contribution to the total conductivity at low temperatures under wet conditions [26]. A similar behavior was encountered for the Ca^{2+} doped system (not shown here), and for the LC compound [17] where protonic defects are the main charge carriers below 400 °C.

In Fig. 6a we present the total conductivity at 10 kHz *vs.* 1/*T* for LCZ50, Ca02LCZ50 and Ca10LCZ50 under wet O_2 (pH_2O = 0.025 atm). The conductivity decreases with increasing level of Ca^{2+}, an effect which becomes more pronounced below approximately 500 °C. Notably, this is the temperature region where protons start to dominate the conductivity. This is further illustrated in Fig. 6b which compares the conductivity values at 800 °C (dominating oxide ion conductivity) and 350 °C (dominating proton conductivity) for different doping levels.

Fig. 7 shows the variations in the total conductivity with φ in wet O_2 (pH_2O = 0.025 atm) at 800 and 350 °C: As the order increases (higher φ value) the conductivities decrease. The most ordered system, Ca02LCZ75 (φ = 0.71), has the lowest oxide ion and proton conductivities among the 1 mol% calcium doped systems (y=0.02), and the proton conductivity decreases even more when the doping level is increased to 5 mol% (Ca10LCZ75).

3.3 TG-DSC

Fig. 8a shows the water uptake, after correction for buoyancy, and the heat flow with respect to sample mass upon hydration at 600 °C as a function of time, for LC [17] and Ca02LCZ75. The shift observed in the DSC baseline upon hydration has been attributed to the change in sample thermal conductivity [18]. A step function was used for the baseline to calculate the area of the DSC peak. It is clear that the height and area of the DSC peak increase with increasing disorder (decreasing φ), representing a more negative enthalpy. Moreover, the water uptake is higher for the more disordered LC (φ = 0.00) than for the more ordered Ca02LCZ75 (φ = 0.71). Fig.8b and 8c show for LC and Ca02LCZ75 as a function of time; on the left y-axis the energy released during hydration representing the integral of the peak in the DSC, and for the right y-axis the molar hydration enthalpy taking the water uptake into account. Evidently, with the low water uptake of these systems, the uncertainty associated with calculating the hydration enthalpy as a function of time becomes large. However, comparing with the values calculated from the standard procedure taking the whole exothermic peak and the water uptake into account, -90 kJ·mol^{-1} for LC and -47 kJ·mol^{-1} Ca02LCZ75, we find the curves in Fig 8b and c acceptable. Fig. 9 presents the hydration enthalpies for all the materials as function of φ and $r_{A^{3+}}/r_{B^{4+}}$ as determined from the TG-DSC data. It should be mentioned that the overall low water uptake in the studied systems relative to the resolution of the TG-DSC instrumentation [28] makes this a more qualitative rather than quantitative analysis to investigate for correlations between φ, hydration enthalpy, and ionic conductivity.

4. Discussion

The total conductivity and the hydration enthalpy across the solid solution series of lanthanum cerate zirconate display interesting features of the level of cation order/disorder and acceptor doping. The compounds studied within the system behave as mixed proton-oxide ion conductors, where protons dominate at the lower temperatures (approx. below 500 °C). Electronic conductivity is essentially negligible in oxidizing atmospheres, but contributes significantly under reducing conditions (pO_2<10^{-20} atm) at higher temperatures. In the following we will discuss the electrical

conductivity and the hydration trends as a function of acceptor doping and Ce/Zr content, and in turn, the order factor φ, in view of the structure and defect chemistry.

Simulation studies of Minervini *et al.* [29] showed that the defects determining the ionic conductivity in undoped $A_2B_2O_7$ arise from anti-Frenkel defect disorder, which consists of oxygen vacancies on 48*f* sites and oxygen interstitials on 8*a* sites (cf. fig. 1b):

$$O^{x}_{O(48f)} = v^{\bullet\bullet}_{O(48f)} + O''_{i(8a)} \quad (3)$$

Under humid environments we may then assume that the oxygen vacancies are hydrated mainly according to:

$$H_2O_{(g)} + v^{\bullet\bullet}_{O(48f)} + O^{x}_{O(48f)} = 2OH^{\bullet}_{O(48f)} \quad (4)$$

Density functional theory calculations (DFT) [30] imply that the formation energy of protons is lowest for the 48*f* site, therefore at this stage we anticipate that the protons are hosted on the 48*f* oxide ions.

As evident from Fig. 7, systems with high degree of cation disorder (low φ) exhibit higher ionic conductivity (both anionic and protonic). Tuller [31] suggested that cation disorder increases the similarity between nonequivalent oxygen sites, namely the 48*f* and the 8*b* sites, facilitating anion disorder and thus promoting anti-Frenkel defect formation (*i.e.* increasing the concentration of intrinsic anion defects, cf. eq. 3). This was later verified by computational studies of Catlow *et al.* [32] and Minervini *et al.* [29]. Consequently, the behavior in Fig. 7 may be rationalized from a defect concentration point of view; a decrease of φ increases the concentration of the intrinsic anion defects, resulting in higher ionic conductivity.

Furthermore, our calculations in ref [30] on formation energies of protons and oxygen vacancies on different oxygen sites for the $La_2B_2O_7$ series (B = Ti, Sn, Zr, Ce) show that when substituting Zr^{4+} with Ce^{4+}, formation of oxygen vacancies on the 8*b* site and oxygen interstitials on the 8*a* is also favorable, in addition to the vacancies at the 48*f* site. The substitution decreases gradually φ and the structure approaches the disordered fluorite in which site exchange between La^{3+}

and Ce^{4+} or Zr^{4+} occurs. A-B site exchange creates an effectively negative charge that is compensated by formation of oxygen vacancies according to:

$$La_2O_3 = 2La'_{Ce,Zr} + v_O^{\bullet\bullet} + 3O_O^x \quad (5)$$

Hence for the disordered oxygen sublattice of the fluorite, the electroneutrality can be described by: $\left[La'_{Ce,Zr}\right] = 2\left[v_{O(8a)}^{\bullet\bullet}\right] + 2\left[v_{O(48f)}^{\bullet\bullet}\right] + 2\left[v_{O(8b)}^{\bullet\bullet}\right]$. We thus regard the fluorite as heavily (50%) La-doped $(Ce,Zr)O_2$. From a conductivity perspective, this increase in the oxygen vacancy concentration provides higher ionic conductivity for the highly disordered systems: LC and systems with high Ce^{4+} content.

Looking at effects on the hydration thermodynamics, Fig 9 presents the hydration enthalpy as a function of the cation order factor, φ. Despite some scatter, the values seem to go through a maximum across the $La_2(Ce_{1-x}Zr_x)_2O_7$ system. For the ordered pyrochlore $La_2Zr_2O_7$ (LZ) the hydration enthalpy obtained both from computational calculations [30] and curve fitting of the conductivity data in [33] is close to -100 ±10 kJ mol^{-1}. From the computations in [30] the hydration enthalpy of LC was estimated to be -57 kJ mol^{-1} when constrained to a fully ordered pyrochlore structure. However, the experimentally measured value for the disordered LC fluorite from TG-DSC, is considerably more exothermic (-90 ± 10 kJ mol^{-1}), highlighting the effect of disorder on the hydration thermodynamics. We attribute the difference in hydration thermodynamics to the higher stability of oxygen vacancies in the ordered pyrochlore compared to the disordered fluorite structure resulting in less favorable hydration. A gradually increase in the stability of the oxygen vacancies, as such, rationalizes the less exothermic hydration with increasing order for higher Zr contents in the fluorite phase region. However, once the pyrochlore structure is attained, changes in the coordination number and bonding nature increasingly favor hydration towards the LZ compound, again yielding more negative enthalpies upon increasing Zr content. All in all, comparing the rather low doping level of the ordered pyrochlore to the disordered fluorite with up to 50% A-B site exchange, a higher maximum hydration and proton concentration level in the disordered than in the ordered materials is expected. In this we tacitly assume that the ordered empty and, thus interstitial, sites of oxygen in the pyrochlore are not

hydrated (cf. Fig 1). They represent an even more stable (lower energy) form of empty oxygen sites than the vacancies in the same pyrochlore, and the enthalpy of this hydration is thus too unfavorable to come into account.

Acceptor doping should, from a concentration point of view, yield an increase in ionic conductivity by oxygen vacancies and protons. Yet, the opposite effect is encountered for the more disordered members of the series; the higher the Ca^{2+} content, the lower the conductivity (cf. Fig. 6). Wen Xing *et al.* [34] recently pointed out that in a system with high degree of cation disorder there may be a limited effect of the doping as it may be compensated by site exchange of cations with different charge, followed by precipitation of an oxide richer in one of them, rather than by the intended formation of mobile charged defects. However, we believe that this is not the explanation in our case, but simply that the additional oxygen vacancies created by Ca-doping are insignificant in comparison to those formed due to the doping caused by the cation disorder (50% La-doped $(Ce,Zr)O_2$). We rationalize that the Ca acceptors actually induce a small negative effect on the conductivity reflects trapping of the charge carriers. This is in line with the higher apparent activation energy, E_a, and pre-exponential, A_0, encountered for Ca doped systems (cf. table 2). It is, finally, interesting to note that for systems with approximately the same φ value (*i.e.* LCZ50, Ca02LCZ50), the hydration enthalpy becomes less exothermic with the increasing Ca^{2+} content (cf. Fig. 9). This behavior may reflect that oxygen vacancies are more strongly trapped at the acceptor dopant site Ca'_{La} [35].

5. Conclusions

In the present study we have discussed the influence of order/disorder on the ionic conductivity in lanthanum cerate/zirconate solid solutions, $(La_{1-y}Ca_y)_2(Ce_{1-x}Zr_x)_2O_{7-\delta}$ (y=0, 0.02, 0.10; x=0, 0.50, 0.75). These compounds are electronic conductors under sufficiently reducing conditions ($pO_2 < 10^{-20}$ atm), but are otherwise mixed proton-oxide ion conductors. Protons are the main charge

carriers at intermediate and low temperatures in the presence of water vapor. Two of the interesting characteristics of these material systems are revealed in the present study. Firstly, an increase in the disorder (decrease of φ) increases the ionic conductivity, both the oxide ion conductivity dominating at higher temperatures and the proton conductivity dominating at lower temperatures giving rise to a more exothermic hydration enthalpy. Secondly, it was found that Ca^{2+} doping decreases the ionic conductivity (both proton and oxide ion conductivity). This was interpreted to reflect trapping of the mobile ions by the acceptor Ca'_{La}.

6. Acknowledgments

Funding from European Union, FP7 EFFIPRO project: *Efficient and robust fuel cell with novel ceramic proton conducting electrolyte* (grant agreement no. 227560) is gratefully acknowledged. The authors also acknowledge the Danish Council for Strategic Research for the funding of the N-INNER project: *Novel High Temperature Proton and Mixed-Proton Electron Conductors for Fuel Cells and H_2-separation membranes* (grant no. 09-064274). The authors thank T. S. Bjørheim at the University of Oslo for valuable discussions

References

[1] K.-D. Kreuer, *Ann. Rev. Mater. Res.* **33** (2003) 333.

[2] K.-D. Kreuer, T. Dippel, Y.M. Baikov, J. Maier, *Solid State Ionics* **86-88** (1996) (Part 1) 613.

[3] K.-D. Kreuer, *Solid State Ionics* **125** (1999) (1-4) 285.

[4] K.-D. Kreuer, S. Adams, W. Münch, A. Fuchs, U. Klock, J. Maier, *Solid State Ionics* **145** (2001) (1-4) 295.

[5] K.H. Ryu, S.M. Haile, *Solid State Ionics* **125** (1999) (1–4) 355.

[6] R. Haugsrud, C. Kjølseth, *J. Phys. Chem. Solids* **69** (2008) (7) 1758.

[7] M. Huse, T. Norby, R. Haugsrud, *J. Electrochem. Soc.* **158** (2011) (8) B857.

[8] R. Haugsrud, T. Norby, *Journal of the American Ceramic Society* **90** (2007) (4) 1116.

[9] G.-y. Adachi, N. Imanaka, S. Tamura, *Chem. Rev.* **102** (2002) (6) 2405.

[10] R. Haugsrud, *Solid State Ionics* **178** (2007) (7-10) 555.

[11] R. Haugsrud, T. Norby, *Nat Mater* **5** (2006) (3) 193.

[12] T. Omata, K. Okuda, S. Tsugimoto, S. Otsuka-Matsuo-Yao, *Solid State Ionics* **104** (1997) (3-4) 249.

[13] Z. Tao, L. Bi, S. Fang, W. Liu, *Journal of Power Sources* **196** (2011) (14) 5840.

[14] B. Lin, S.L. Wang, X.Q. Liu, G.Y. Meng, *Journal of Alloys and Compounds* **478** (2009) (1-2) 355.

[15] P.K. Moon, PhD Thesis, Massachusetts Institute of Technology (1988).

[16] J.A. Díaz-Guillén, M.R. Díaz-Guillén, K.P. Padmasree, A.F. Fuentes, J. Santamaría, C. León, *Solid State Ionics* **179** (2008) (38) 2160.

[17] V. Besikiotis, C.S. Knee, I. Ahmed, R. Haugsrud, T. Norby, *accepted for publication in Solid State Ionics* http://dx.doi.org/10.1016/j.ssi.2012.08.023.

[18] C. Kjølseth, L.Y. Wang, R. Haugsrud, T. Norby, *Solid State Ionics* **181** (2010) (39-40) 1740.

[19] A. Le Bail, H. Duroy, J.L. Fourquet, *Materials Research Bulletin* **23** (1988) (3) 447.

[20] http://www.ill.eu/sites/fullprof/.

[21] Program for the Collection and the Evaluation of X-ray Powder Data, Stoe & Cie. GmbH, Darmstadt (1999).

[22] B.A. Boukamp, Equivalent Circuit for Windows v. 1.0, (2003).

[23] S.M. Haile, D.L. West, J. Campbell, *Journal of Materials Research* **13** (1998) (6) 1576.

[24] B.A. Boukamp, *Solid State Ionics* **20** (1986) (1) 31.

[25] S. Ricote, N. Bonanos, H.J. Wang, R. Haugsrud, *Solid State Ionics* **185** (2011) (1) 11.

[26] A.S. Nowick, A.V. Vaysleyb, *Solid State Ionics* **97** (1997) (1-4) 17.

[27] N. Bonanos, *Solid State Ionics* **53-56** (Part 2) 967.

[28] C. Kjølseth, PhD Thesis University of Oslo (2009).

[29] L. Minervini, R. W. Grimes, K. E. Sickafus, *Journal of the American Ceramic Society* **83** (2000) (8) 1873.

[30] T. S. Bjørheim, V. Besikiotis, R. Haugsrud, *under review Dalton Trans.* (2012).

[31] H.L. Tuller, *J. Phys. Chem. Solids* **55** (1994) (12) 1393.

[32] P.J. Wilde, C.R.A. Catlow, *Solid State Ionics* **112** (1998) (3-4) 173.

[33] H. Haug, *internal report* (2008).

[34] W. Xing, K. Toyoura, T. Norby, *International Journal of Hydrogen Energy* (2011).

[35] K. Momma, F. Izumi, *Journal of Applied Crystallography* **41** (2008) (3) 653.

Tables caption:

Table 1*:* System abbreviation, empirical cation disorder factor (φ) and radii ratio.

Table 2*:* Proton conductivity parameters as a function of Ca^{2+} doping.

Figures caption:

Figure 1: Schematic representation [35] of the arrangements of cations A (medium) and B (small), oxygen anions (large) and oxygen vacancies (white): (a) disordered fluorite (b) pyrochlore. For sake of illustration the random assemblage of A and B cations has been marked with the double colored (grey-light grey) balls.

Figure 2: XRD patterns (a) in 2θ range of 25-70° for the studied systems, (b) the (622) and (444) peaks in 2θ range of 54.5-59° for Ca02LCZ50 and Ca02LCZ75. The diffractograms have been shifted vertically in the figures for clarity.

Figure 3: Impedance spectra of Ca02LCZ50 and Ca10LCZ50 recorded at 400 °C under wet O_2 (pH_2O = 0.025 atm).

Figure 4: pO_2 dependences of the total conductivity at 800 °C for the $(La_{1-y}Ca_y)_2(Ce_{1-x}Zr_x)_2O_{7-\delta}$ systems (pH_2O = 0.025 atm).

Figure 5: Total conductivity (left axis) and conductivity ratio between wet and deuterated oxygen (right axis) *vs.* inverse temperature for LCZ50.

Figure 6: Total conductivity under wet O_2 (pH_2O = 0.025 atm) *vs.* (a) inverse temperature for the undoped and acceptor doped $La_2Ce_{1.50}Zr_{0.50}O_7$, and (b) *vs.* Ca^{2+} content at 800 °C (dominating oxide ion conductivity) and 350 °C (dominating proton conductivity).

Figure 7: Total conductivity of $(La_{1-y}Ca_y)_2(Ce_{1-x}Zr_x)_2O_{7-\delta}$ (y=0, 0.02, 0.10 and x=0, 0.50, 0.75) *vs.* cation order factor φ at 800 °C (dominating oxide ion conductivity) and 350 °C (dominating proton conductivity). under wet O_2, pH_2O = 0.025 atm.

Figure 8: (a) DSC and water uptake signals at 600 °C for LC [17] and Ca02LCZ75,(b) LC, and (c) Ca02LCZ75 released energy (left axis) and hydration enthalpy (right axis) *vs*. time.

Figure 9: Hydration enthalpy, ΔH^0_{Hyd}, determined from TG-DSC measurements for $(La_{1-y}Ca_y)_2(Ce_{1-x}Zr_x)_2O_{7-\delta}$ (y=0, 0.02, 0.10 and x=0, 0.50, 0.75), *vs.* cation order factor φ and $r_{A^{3+}} / r_{B^{4+}}$ .The hydration enthalpy for LZ is from computational calculations [30] and curve fitting of the experimental data [33].

	Apparent activation energy, $^{*}E_a$ / eV	Pre-exponential, $A_0 \cdot 10^5$ / K·S·cm^{-1}	Ionic conductivity, σ_{ion} at 350 °C / S·cm^{-1}
LCZ50	0.89	1.09	$4.6 \cdot 10^{-6}$
Ca02LCZ50	0.97	2.4	$2.5 \cdot 10^{-6}$
Ca10LCZ50	0.98	2.8	$2.0 \cdot 10^{-6}$

Table 1: System abbreviation, empirical cation disorder factor (φ) and radii ratio.

System	Abbreviation	φ	$r_{A^{3+}} / r_{B^{4+}}$
$La_2Ce_2O_7$	LC	0.00	1.33
$La_2Ce_{1.50}Zr_{0.50}O_{7-\delta}$	LCZ50	0.46	1.46
$La_{1.98}Ca_{0.02}Ce_{1.50}Zr_{0.50}O_{7-\delta}$	Ca02LCZ50	0.46	1.46
$La_{1.90}Ca_{0.10}Ce_{1.50}Zr_{0.50}O_{7-\delta}$	Ca10LCZ50	0.43	1.45
$La_{1.98}Ca_{0.02}Ce_{1.25}Zr_{0.75}O_{7-\delta}$	Ca02LCZ75	0.71	1.53
$La_{1.90}Ca_{0.10}Ce_{1.25}Zr_{0.75}O_{7-\delta}$	Ca10LCZ75	0.71	1.53
$La_2Zr_2O_7$ [29],[32]	LZ	1.00	1.61

Table 2: Proton conductivity parameters as a function of Ca^{2+} doping.

* The apparent activation energy E_a and pre-exponential factor A_0 are extracted from curve fitting of the conductivity data for the temperature range 500-300 °C.

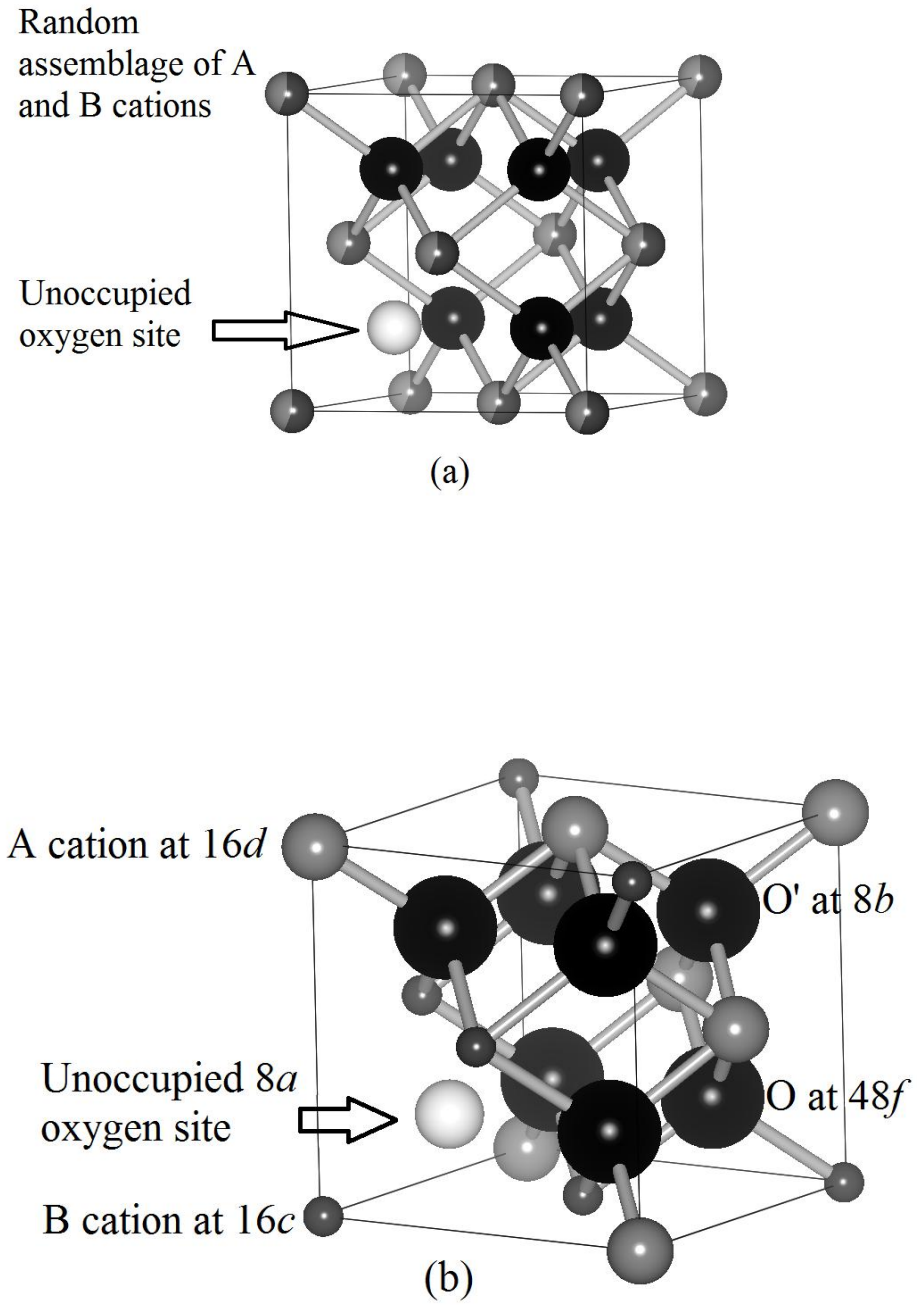

Figure 1. Schematic representation [34] of the arrangements of cations A (medium) and B (small), oxygen anions (large) and oxygen vacancies (white): (a) disordered fluorite (b) pyrochlore. For sake of illustration the random assemblage of A and B cations has been marked with the double colored (grey-light grey) balls.

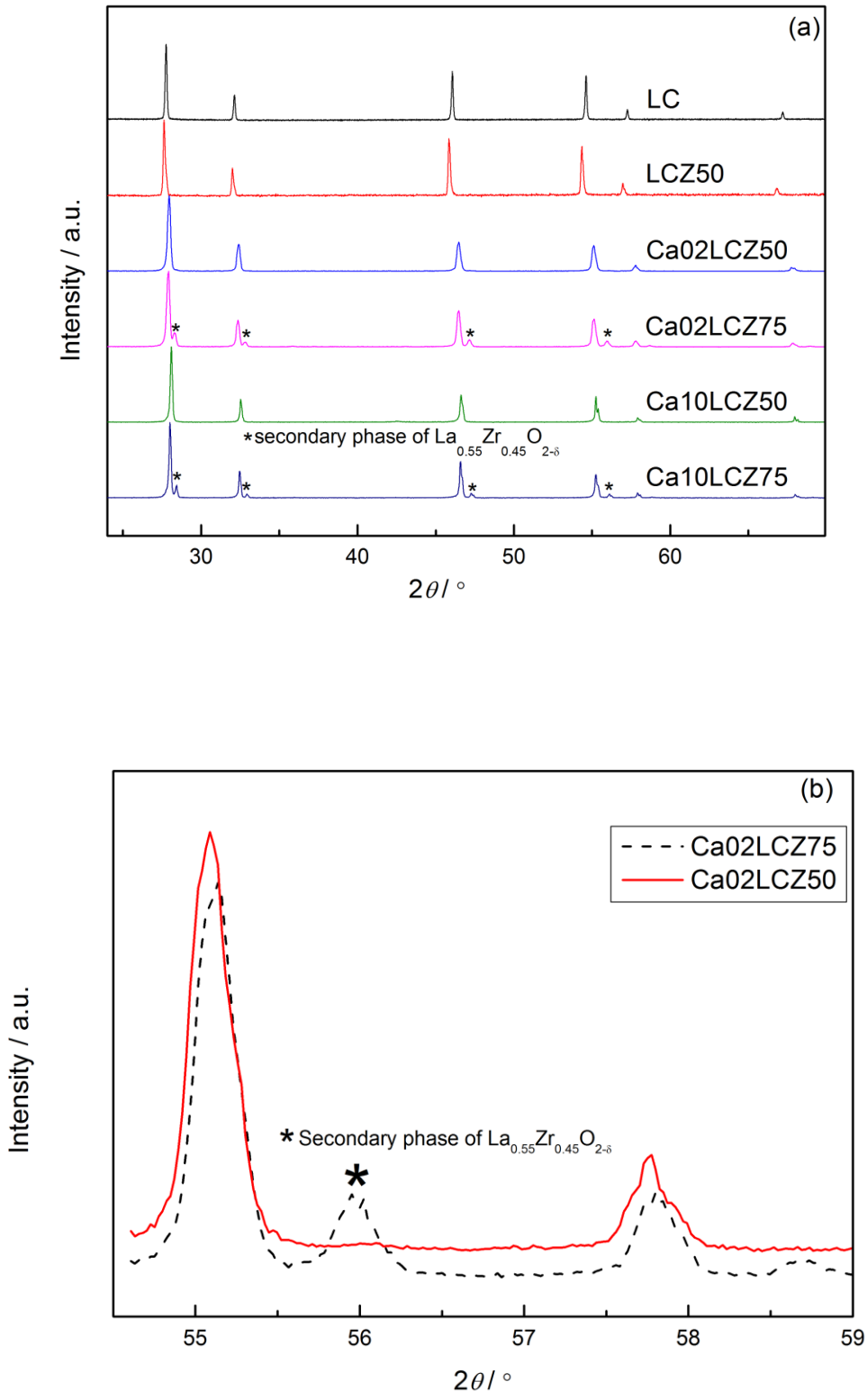

Figure 2. XRD patterns (a) in 2θ range of 25-70° for the studied systems, (b) the (622) and (444) peaks in 2θ range of 54.5-59° for Ca02LCZ50 and Ca02LCZ75. The diffractograms have been shifted vertically in the figures for clarity.

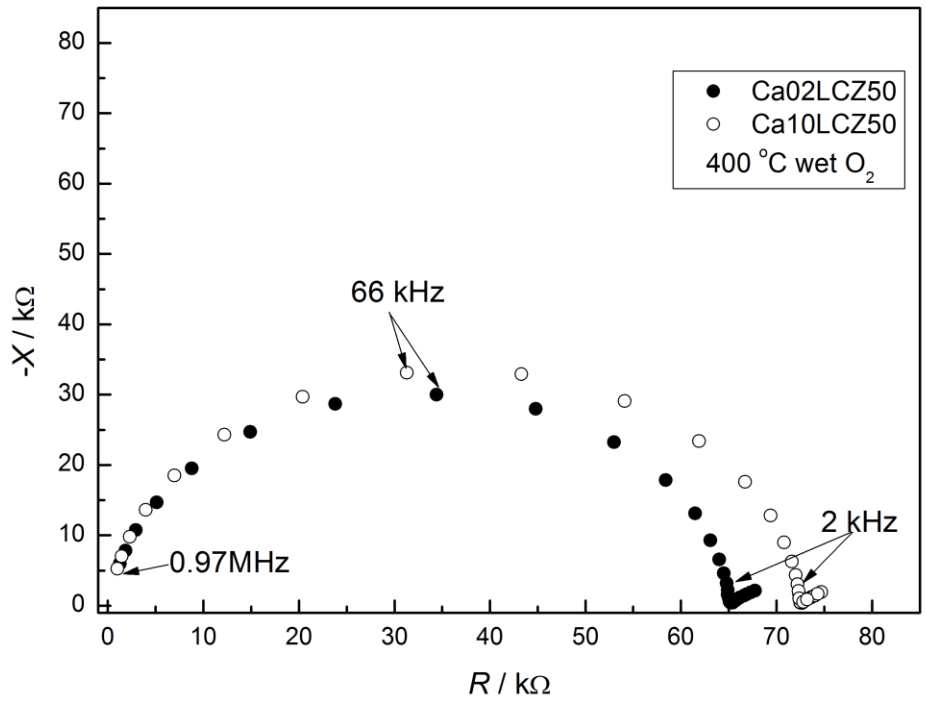

Figure 3. Impedance spectra of Ca02LCZ50 and Ca10LCZ50 recorded at 400 °C under wet O_2 (pH_2O = 0.025 atm).

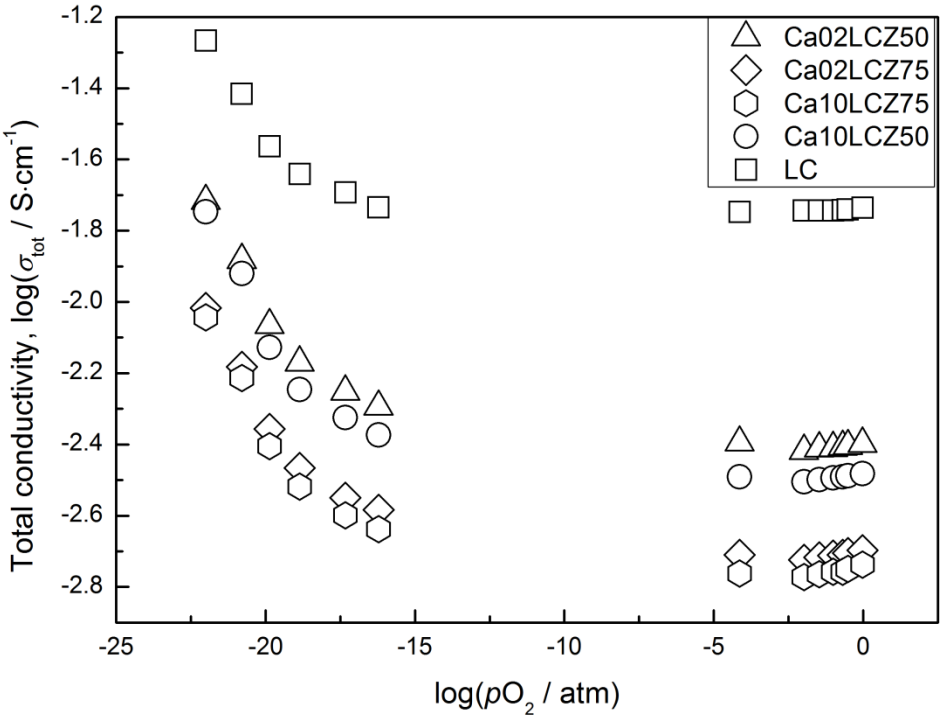

Figure 4. pO_2 dependences of the total conductivity at 800 °C for the $(La_{1-y}Ca_y)_2(Ce_{1-x}Zr_x)_2O_{7-\delta}$ systems (pH_2O = 0.025 atm).

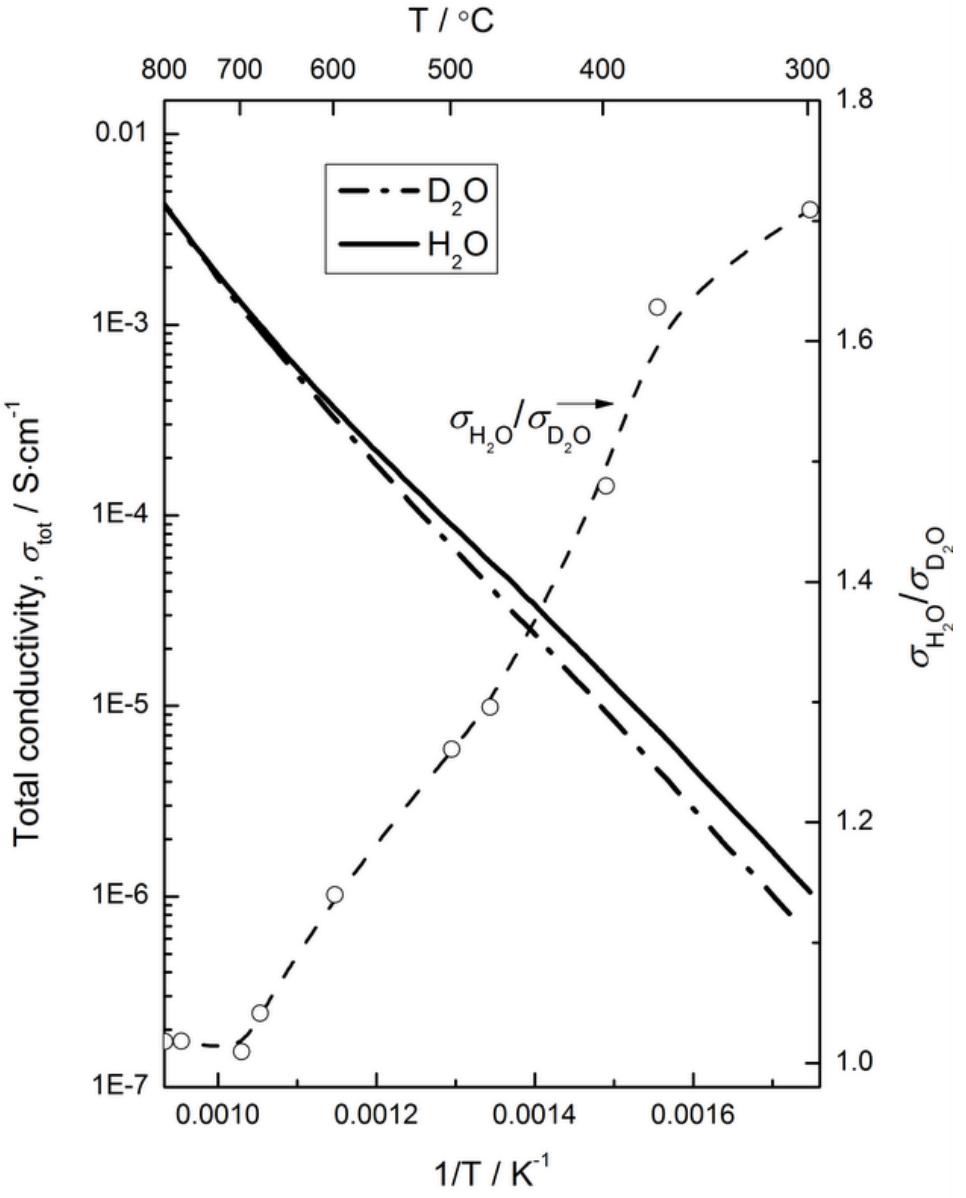

Figure 5. Total conductivity (left axis) and conductivity ratio between wet and deuterated oxygen (right axis) *vs.* inverse temperature for LCZ50.

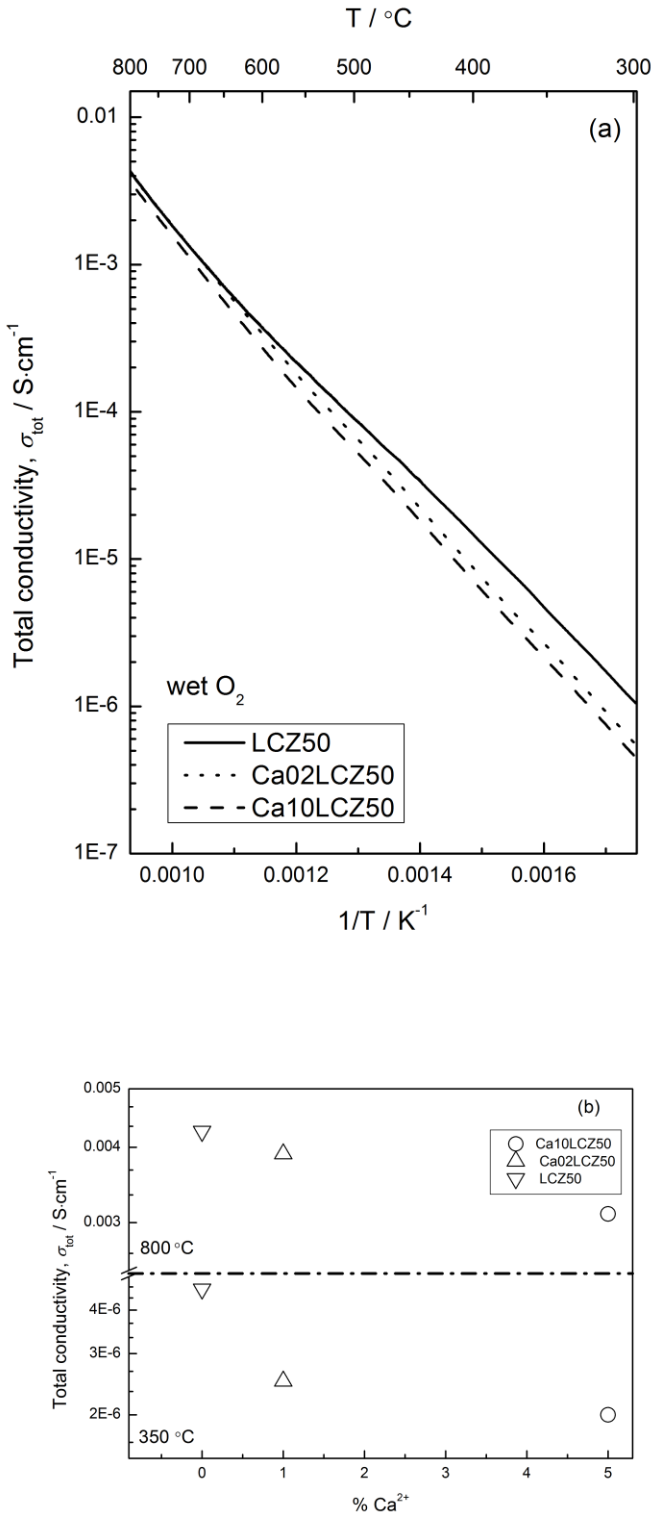

Figure 6. Total conductivity under wet O_2 (pH_2O = 0.025 atm) *vs.* (a) inverse temperature for the undoped and acceptor doped $La_2Ce_{1.50}Zr_{0.50}O_7$, and (b) *vs.* Ca^{2+} content at 800 °C (dominating oxide ion conductivity) and 350 °C (dominating proton conductivity).

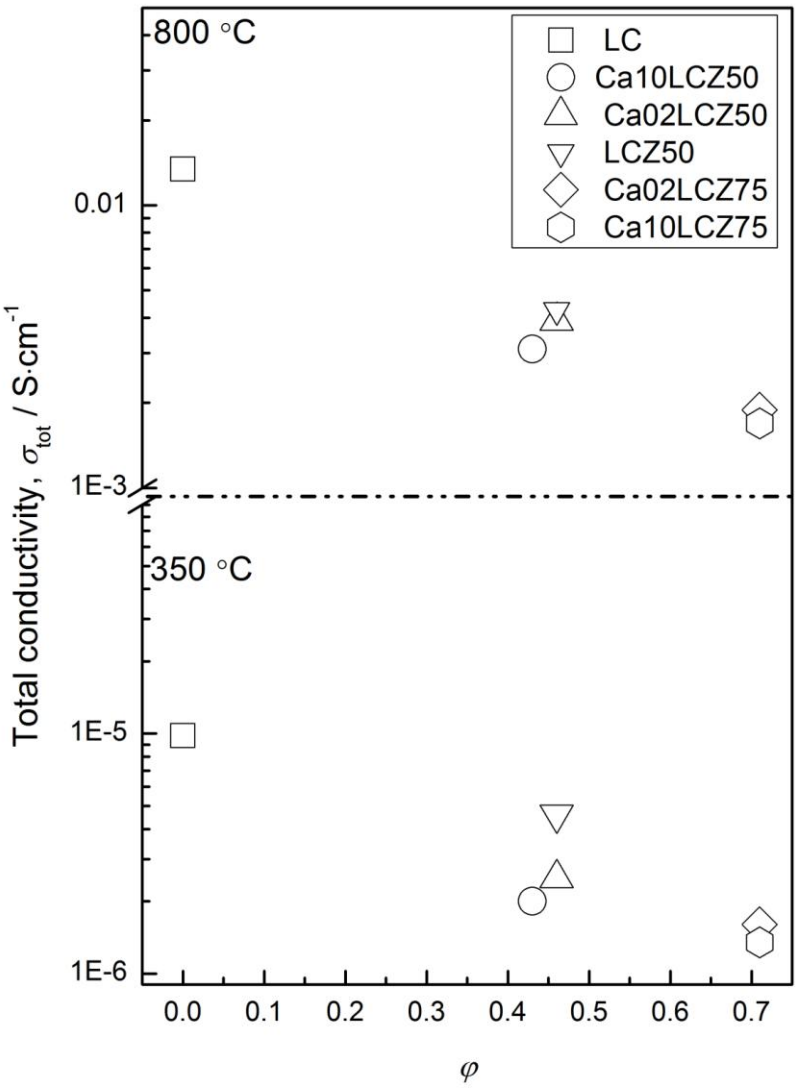

Figure 7. Total conductivity of $(La_{1-y}Ca_y)_2(Ce_{1-x}Zr_x)_2O_{7-\delta}$ (y=0, 0.02, 0.10 and x=0, 0.50, 0.75)*vs.* cation order factor φ at 800 °C (dominating oxide ion conductivity) and 350 °C (dominating proton conductivity). under wet O_2, pH_2O = 0.025 atm.

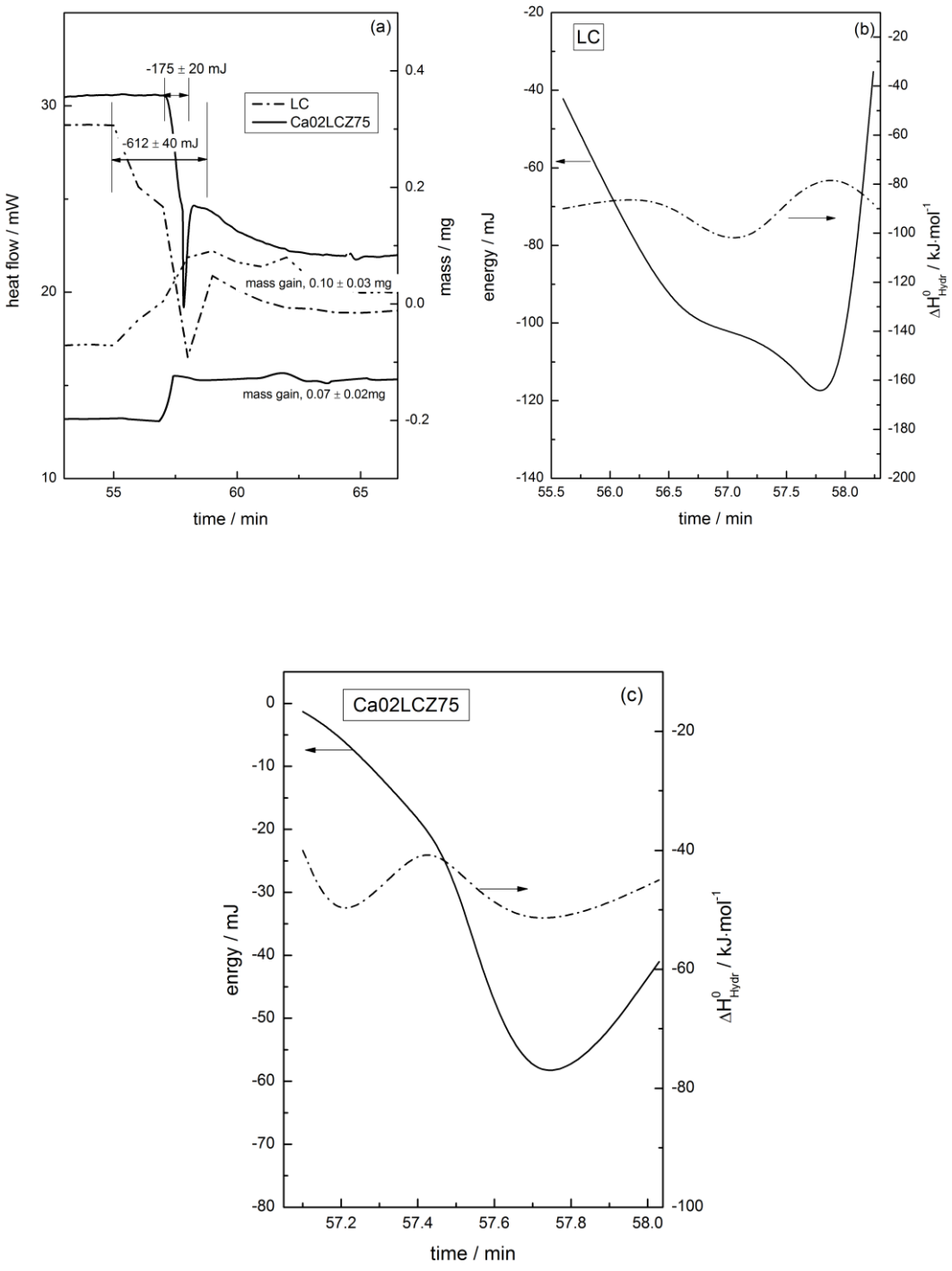

Figure 8. (a) DSC and water uptake signals at 600 °C for LC [17] and Ca02LCZ75,(b) LC, and (c) Ca02LCZ75 released energy (left axis) and hydration enthalpy (right axis) *vs*. time.

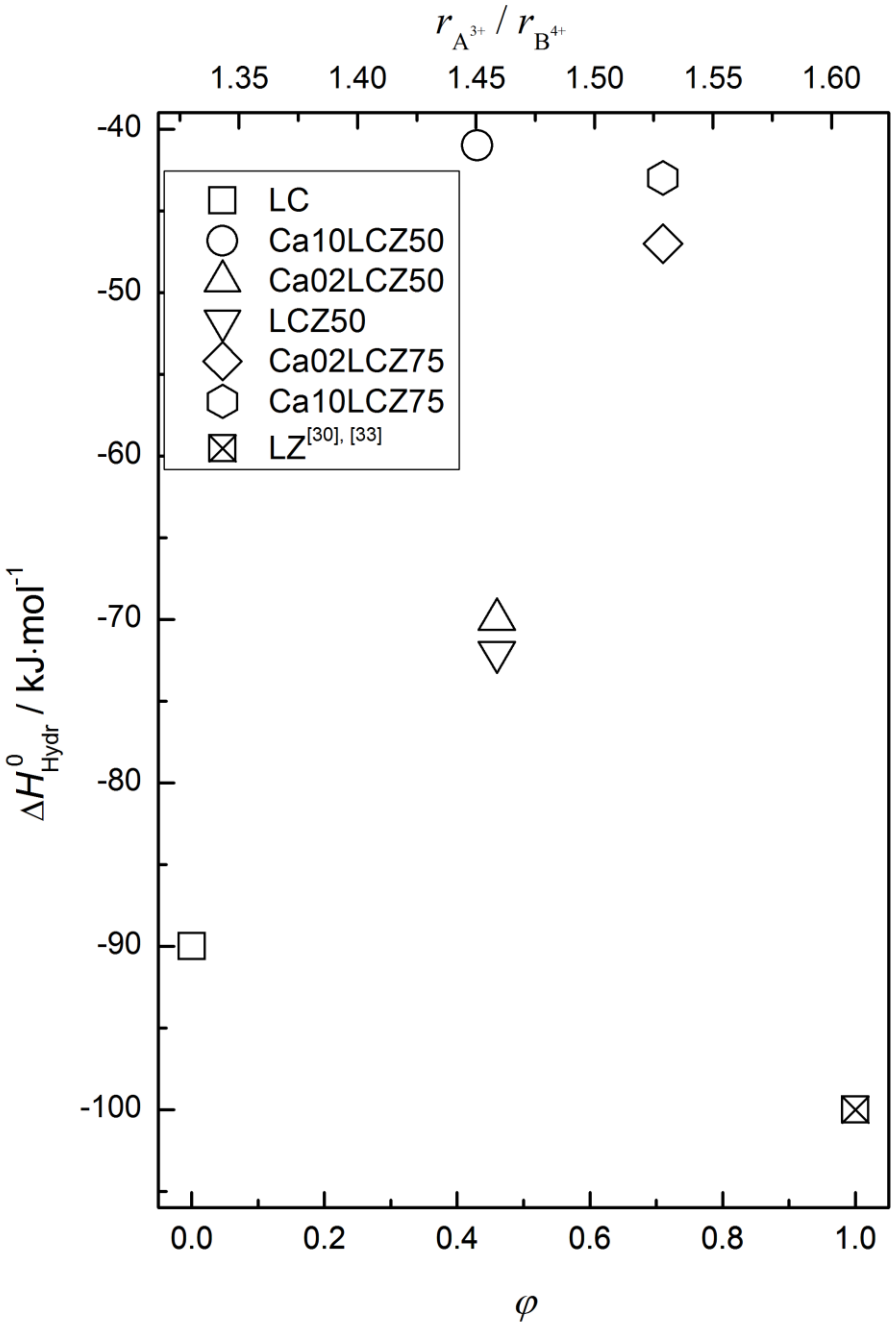

Figure 9. Hydration enthalpy, ΔH^0_{Hyd}, determined from TG-DSC measurements for $(La_{1-y}Ca_y)_2(Ce_{1-x}Zr_x)_2O_{7-\delta}$ (y=0, 0.02, 0.10 and x=0, 0.50, 0.75), *vs.* cation order factor φ and $r_{A^{3+}} / r_{B^{4+}}$ .The hydration enthalpy for LZ is from computational calculations [30] and curve fitting of the experimental data [33].